

DR WENWEI GE (Orcid ID : 0000-0001-7845-2267)

PROFESSOR LAIHUI LUO (Orcid ID : 0000-0002-2370-8277)

Article type : Article

Combining effects of TiO_6 octahedron rotations and random electric fields on structural and properties in $\text{Na}_{0.5}\text{Bi}_{0.5}\text{TiO}_3$

Kaijun Hao¹, Wenwei Ge^{1,†}, Zhenan Ren¹, Xiaojuan Liu⁴, Laihui Luo⁵, Xiaobing Li⁶, Haosu Luo³ and D. Viehland²

¹Key Laboratory of Automobile Materials of Ministry of Education & School of Materials Science and Engineering, Jilin University, Changchun, Jilin 130022, China

²Department of Materials Science and Engineering, Virginia Tech, Blacksburg, Virginia 24061, USA

³Shanghai Institute of Ceramics, Chinese Academy of Sciences, Shanghai 201800, China

⁴State Key Laboratory of Rare Earth Resource Utilization, Changchun Institute of Applied Chemistry, Chinese Academy of Sciences, Changchun 130022, China

⁵Department of Microelectronic Science and Engineering, Ningbo University, Ningbo, 315211, China

⁶School of Medical Instrument and Food Engineering, University of Shanghai for Science and Technology, 516 Jungong Road, Yangpu, Shanghai 200093, China

This is the author manuscript accepted for publication and has undergone full peer review but has not been through the copyediting, typesetting, pagination and proofreading process, which may lead to differences between this version and the [Version of Record](#). Please cite this article as [doi: 10.1111/JACE.16986](https://doi.org/10.1111/JACE.16986)

This article is protected by copyright. All rights reserved

Abstract

The structural and dielectric properties of $\text{Na}_{0.5}\text{Bi}_{0.5}\text{TiO}_3$ (NBT) ceramics and crystals have been investigated and are compared to that of $\text{Pb}(\text{Zr}_{0.55}\text{Ti}_{0.45})\text{O}_3$ (PZT 55/45) and $\text{Pb}(\text{Mg}_{1/3}\text{Nb}_{2/3})_{0.72}\text{Ti}_{0.28}\text{O}_3$ (PMNT 72/28) ceramics. XRD profiles for (100), (110), (111), (200), (220) and (222) (referred to cubic structure) reveal that the monoclinic structure with Cc space group exists both in NBT single crystal and ceramics. The diffraction profile obtained with high resolution lab XRD for NBT single crystal can be well described using Cc model instead of $R3c$ model. The dielectric constant of NBT below T_{hump} shows some similarity to that of PZT 45/55 ceramics below 50°C in which oxygen octahedron rotations cause the frequency dispersion of the dielectric constant. The temperature dependent dielectric constant for NBT can be deconvolved into two independent processes. The lower temperature process shows a typical relaxor characteristic and follows the Vogel-Fulcher relationship. The other process at higher temperature shows less frequency dependent behavior. Comparing dielectric constant of NBT with that of PZT55/45 and PMNT72/28 reveals that both oxygen octahedral rotations and random electric fields play important role in the frequency dispersion of the dielectric constant for NBT relaxor ferroelectric.

† Author to whom correspondence should be addressed. Electronic mail: wenweige@jlu.edu.cn

I. Introduction

Sodium bismuth titanate ($\text{Na}_{0.5}\text{Bi}_{0.5}\text{TiO}_3$ or NBT) is a potential lead-free alternative to lead-based piezoelectric materials because it can form solid solutions with many other compounds to enhance piezoelectric properties near a morphotropic phase boundary (MPB) compositions.(1-4) NBT is a relaxor ferroelectric with A sites of perovskite occupied by random mixtures of heterovalent cations Na^+ and Bi^{3+} which makes NBT is different from prototype relaxors, such as $\text{Pb}(\text{Mg}_{1/3}\text{Nb}_{2/3})\text{O}_3$ (PMN) and $\text{Pb}(\text{Mg}_{1/3}\text{Nb}_{2/3})\text{O}_{3-x}\% \text{PbTiO}_3$ (PMNT(100- x)/ x) in which B sites of perovskite are occupied by random mixtures of heterovalent cations.(5, 6) Temperature dependent dielectric constant ϵ_r of relaxor ferroelectric PMN shows strong frequency dispersion before a temperature T_{\max} where a broad dielectric maximum occurs: the T_{\max} shifts toward high temperature and ϵ_r decreases with increasing frequency (ω).(7) (T_{\max} , ω) can be modeled with the Vogel-Fulcher relationship.(8) It is proposed that the relaxor behavior of PMN can be related to a short range ordered polar nano-regions (PNRs) resulted from random electric fields (REFs) because the B sites of perovskite are occupied by random mixtures of heterovalent cations.(9) With temperature increasing, the correlation length of PNRs decreases and the PNRs transformed into smaller, randomly oriented and very local polar regions above the T_{\max} . When the temperature further increases to a so called Burns temperature T_d , the local polarization disappears and the relaxor ferroelectrics begin to follow the Curie-Weiss law above the T_d .(10, 11) The existence of PNRs are evidenced by the observation of temperature dependent strong neutron diffuse scattering around Bragg peaks in reciprocal space for relaxors ferroelectrics below the T_d when measured with thermal neutrons. (12) However, the relaxor behavior in NBT is different from that in PMN. For NBT, temperature dependent ϵ_r curve shows two dielectric abnormal temperatures on heating in the temperature range from room temperature to high temperature: T_{hump} (~ 250 °C) and T_{\max} (~ 330 °C). (13) The ϵ_r between T_{hump} and T_{\max} is almost frequency independent, while the ϵ_r below T_{hump} shows frequency dispersion behavior in NBT.

The structural phase transformation is also quite different in NBT and PMN.
This article is protected by copyright. All rights reserved

PMN does not show any long-range structural distortion under zero electric field at low temperatures except that short-range polar correlations appear giving rise to strong neutron diffuse scattering. (7, 14) When PMN is doped with PT to form PMNT(100-x)/x solid solutions, there is a MPB region between rhombohedral ($R3m$) and tetragonal ($P4mm$) phases in the vicinity of $x \approx 30$. (15) Depending on electric field and thermal history, high resolution x-ray diffraction studies revealed different monoclinic phases (Pm or Cm) existing near the MPB composition of PMNT(100-x)/x solid solutions. (16, 17) The monoclinic phase is believed to play an important role bridging rhombohedral and tetragonal phases via polarization rotation, (18) which gives rise high piezoelectricity near the MPB in Pb-based piezoelectric materials. (19-21) Comparing PMN and NBT shows complicated structural phase transitions in NBT. It was reported that NBT undergoes a phase transition sequence of cubic (C, $Pm\bar{3}m$) $\xrightarrow{\sim 540^\circ\text{C}}$ tetragonal (T, $P4bm$) $\xrightarrow{\sim 260^\circ\text{C}}$ rhombohedral (R, $R3c$). (22) The T ($P4bm$) structure is distorted from cubic by in-phase rotations of the TiO_6 octahedra about the $[001]_{\text{PC}}$ (referred to perovskite cubic), according to the tilt system $a^0a^0c^+$ (Glazer notation (23)), combined with antiparallel displacement of the $\text{Na}^{1+}/\text{Bi}^{3+}$ and Ti^{4+} cations along $[001]_{\text{PC}}$. The R ($R3c$) structure is characterized by a^-a^- (Glazer notation (23)) antiphase octahedral rotations about $[111]_{\text{PC}}$, combined with parallel displacement of the $\text{Na}^{1+}/\text{Bi}^{3+}$ and Ti^{4+} cations along the $[111]_{\text{PC}}$ axis. (22) Recent high-resolution synchrotron x-ray powder diffraction studies of NBT ceramics (24, 25) and crystals (26) have indicated that the room-temperature structure of NBT is the monoclinic (M) of space group Cc with a tilt system of $a^-a^-c^-$ rather than rhombohedral $R3c$ with the tilt system of a^-a^- . Nevertheless, both Cc and $R3c$ structures have anti-phase oxygen octahedron rotations but they give rising superlattice diffraction peaks at different 2θ positions. (27)

Oxygen octahedron rotation occurs often in perovskites as it allows energy minimization by change the bond length and angles, particularly when perovskites are under high pressures (28, 29) or low temperatures. (27, 30) It has been argued that random electric fields (REFs) play an essential role in establishing the relaxor

phase(31-35) even though some theoretical works suggest relaxor behavior can occur in the absence of REFs. (36-38) However, the influences of oxygen octahedron rotation on the relaxor behaviors are seldom reported due to the lack of oxygen octahedron rotation for most Pb-based relaxors at ambient conditions. (39) Dai *et al.* reported a frequency dispersion of dielectric constant of PZT ceramics with Zr/Ti ratios between 95/5 and 55/45 at low temperatures where oxygen octahedron rotation phase existed. (30) Such low temperature oxygen octahedron rotation phase was determined to be *Cc* structure coexisting with *Cm* phase in PZT52/48 ceramics. (27) It is believed that PZT solid solutions have much weaker REFs compared to PMN because *B* sites of perovskite are occupied by homovalent cations. A remarkable peculiarity of the NBT is that oxygen octahedron rotation and heterovalent cations of Na^+ and Bi^{3+} occupying on the *A* sites of perovskite simultaneously exist at ambient conditions, which leads to some controversial arguments about the *E*-field induced phase transformation near the MPB in NBT-based solid solutions. (40) Thus NBT provides a unique opportunity to investigate the combining effect of oxygen octahedron rotation and REFs in relaxors, which may shed new light on the understanding of relaxor behavior in NBT compared to PMN.

Here, we report a comparison dielectric study of NBT (crystals and ceramics), PMNT72/28 (ceramics) and PZT55/45 (ceramics). The structure of NBT (crystals and ceramics) was also investigated by using conventional lab XRD because the *M* phase in NBT determined by conventional lab XRD has not been reported yet. (41) We found that both NBT crystals and ceramics show clear evidence of *M* (*Cc*) phase. With increasing temperature, the frequency dispersion of dielectric constant was strongly enhanced in PMNT72/28 ceramics and moderate enhanced in NBT crystals and ceramics, while it was slightly decreased in PZT55/45 ceramics.

II. Experimental Procedure

Ceramics of NBT and PMNT72/28 were prepared through a conventional solid state reaction method with raw materials of Na_2CO_3 (AR), Bi_2O_3 (AR), TiO_2 (CP), PbO (AR), MgO (AR), and Nb_2O_5 (2.5N) produced by Tianjin Kemiou Chemical Reagent Co. or Sinopharm Chemical Reagent Co. (SCRC). The raw materials had

been dried at 120°C for 1.5hr to remove any moisture absorbed from the air before they were weighed according to the mole ratios of NBT and PMNT72/28. All the raw materials were weighed, mixed with ethanol and ball milled for 1hr. Then the mixed raw materials were dried and calcined to obtain ceramic powders. For PMNT72/28 ceramics, two-step solid state reaction method(42) was chosen to avoid the pyrochlore phase: the calcine temperatures for obtaining $MgNb_2O_6$ and PMNT72/28 is 1100°C and 900°C, respectively. For NBT, the mixed raw materials were dried and calcined at 900°C for 3 hr. Then the calcined ceramic powders of NBT and PMNT72/28 were ground and ball milled again for 6 hr. Then they were mixed with 3% PVA as binder and made into green body with dimensions of $\Phi 10\text{mm} \times 2\text{ mm}$ under a uniaxial pressure of 200 MPa. At last, the green body was heated and hold at 500°C for half an hour to burn out the PVA and then sintered at 1100°C for 2hr. The sintered NBT and PMNT72/28 ceramics were polished to ensure parallel surfaces. Silver electrodes were fired on both parallel surfaces of the ceramics for dielectric measurement. Single crystals of NBT were grown by a top-seeded solution growth method. (43) Pseudocubic $\langle 001 \rangle$ oriented NBT crystal wafers with thicknesses of 0.7 mm were cut from a boule, and subsequently electroded with Pt on both surfaces. Temperature dependent dielectric constant measurements were performed using a LCR meter (HP 4284A) and DMS-500 (Partulab) under zero-field heating conditions in the temperature range of 30°C to 400°C. X-ray diffraction studies for NBT crystal were performed using a Philips MPD high-resolution X-ray diffraction system, equipped with a two bounce hybrid monochromator, an open three-circle Eulerian cradle, and a domed hot-stage. A Ge (220)-cut crystal was used as an analyzer. The X-ray wavelength was that of $CuK\alpha$, i.e. 1.5406 Å and the x-ray generator was operated at 45 kV and 40 mA. X-ray diffraction data for NBT ceramic pellets were collected on a Rigaku D/max-2500/PC system equipped with copper target and graphite monochromator. The ratios for $CuK\alpha_2/CuK\alpha_1$ is ~ 0.5 and the X-ray generator was operated at 50 kV and 200 mA. The 2θ step size and scan speed were (0.01°, 1°/min) and (0.001°, 0.06°/min) for NBT ceramics and crystals during data collection. The diffraction peaks corresponding to $(100)_{PC}$, $(110)_{PC}$, $(111)_{PC}$, $(200)_{PC}$, $(220)_{PC}$ and

(222)_{PC} reflections were fitted by using software of OriginPro (Originlab, Inc.). The $\text{CuK}\alpha_2$ line in the diffraction data for NBT ceramics were stripped by using Jade software before peak fitting.

III. Results and discussions

(1). Monoclinic Cc structure for NBT single crystals and ceramics

Figures 1(a-f) show the x-ray diffraction profiles for NBT single crystals around (100)_{PC}, (110)_{PC} and (111)_{PC} (a-c on left column) and (200)_{PC}, (220)_{PC} and (222)_{PC} (d-f on right column). Corresponding to (100)_{PC}, a strong diffraction peak was observed near $2\theta \approx 22.9^\circ$ which showed a slight distortion on the right side of the peak as shown in the Fig.1(a). Fig.1(d) is the (200)_{PC} diffraction peak which clearly shows two peaks on the top and partly overlapped at the bottom. These results are consistent with that the distortion of XRD peaks at low 2θ angle will become more obvious and even to lead to peak splitting at high 2θ angle. The distortion and splitting on (100)_{PC} and (200)_{PC} diffraction peaks are favor Cc structure but against R3c structure which has only one single peak for both (100)_{PC} and (200)_{PC} diffractions. All the diffraction peaks were deconvolved using Voigt function according to monoclinic Cc structure as shown in the Figs.1(a-f). The observed XRD profiles can be well described by the calculated profiles and the goodness of fit (*R*-Square) is higher than 0.99. The fitted 2θ value and calculated *d*-spacing are listed in Table I. The 1st column of the Table I shows reflection index (*h k l*) for Cc structure. The 2θ value corresponding to (*h k l*) and ($2h\ 2k\ 2l$) are listed in the 2nd and 4th column of the Table I. Then the *d*-spacing for (*h k l*) and ($2h\ 2k\ 2l$) reflections are calculated according to the fitted 2θ and shown in the 3rd and 5th column of the Table I. The last column of the Table I shows the ratios of *d*-spacing for (*h k l*) and ($2h\ 2k\ 2l$) reflections which are almost close to the ideal value of 2. These results strongly suggest that the deconvolution of XRD peaks of NBT crystal according to Cc structure is a good fit. The calculated monoclinic lattice parameters (*a, b, c, β*)=(9.5201 Å, 5.4846 Å, 5.5024 Å, 125.3542 °) for Cc structure are listed in the bottom row of the Table I, which are very close to that of (*a, b, c, β*)=(9.5261 Å, 5.4831 Å, 5.5079 Å, 125.3442 °) obtained by high resolution synchrotron x-ray diffraction on ceramics powders. (24) During XRD

This article is protected by copyright. All rights reserved

measurements on NBT single crystal, the x-ray generator was operated at a low power of 1.8kW, which is difficult to measure the superlattice reflections result from oxygen octahedral rotation in NBT.

Previous reported Cc structure for NBT is limited to synchrotron x-ray diffraction results which are high resolution and high intensity. (24, 26) Following neutron diffraction results reported by Jones, (22) XRD results obtained by conventional lab x-ray diffraction for NBT were generally interpreted as $R3c$ structure partially because the peak distortion or splitting were quite small as can be seen in the Table I. The conventional lab XRD data for NBT ceramics were carefully collected at a 2θ step size of 0.01° and the x-ray generator was operated at a power of 10kW in this work. Fig. 2(a) shows the XRD data in the 2θ range of $10^\circ \sim 90^\circ$. All the diffraction peaks belong to perovskite phase without any other phases detected within the limit of the x-ray diffraction meter. Figs. 2(b-d) shows the enlarged parts of the Fig.2(a) corresponding to the $(110)_{PC}$, $(111)_{PC}$ and $(200)_{PC}$ diffraction peaks which are the three strongest peaks among all the diffraction peaks except $(211)_{PC}$ peak near the 57° . Though the signal/noise ratio and resolution of the observed XRD data obtained from conventional lab XRD are lower and coarser than that of single crystal diffraction data or synchrotron x-ray diffraction data, the distortion on the left bottom of $(200)_{PC}$ is ready to see in the Fig.2(d). These results obtained on conventional lab XRD for NBT ceramics favor Cc instead of $R3c$ structure. The diffraction peaks were deconvolved using Voigt function according to monoclinic Cc structure as it was done for NBT crystal previously, as shown in the Figs.2(b-d). The fitted 2θ value and calculated d -spacing are listed in Table II. The lattice parameters for monoclinic Cc structure were calculated to be $(a, b, c, \beta) = (9.6660 \text{ \AA}, 5.4958 \text{ \AA}, 5.5815 \text{ \AA}, 126.3090^\circ)$, respectively. The calculated d -spacing and lattice parameters for NBT ceramics are bigger than that of NBT crystals but the differences are less than 1% and 2%, as shown in the last column of the Table II. These differences can be partially attributed to the coarser resolution of the conventional lab XRD comparing to the high resolution diffraction meter equipped with crystal monochromator for $CuK\alpha_1$ radiation.

The superlattice reflections of $(1/2, 1/2, 1/2)_{PC}$ is only allowed for *Cc* structure while the $(3/2, 1/2, 1/2)_{PC}$ are allowed for both *Cc* and *R3c* structures. It can be seen that only background data were observed in the dashed rectangle in the inset (e) of the Fig.2(a) where the superlattice reflections of $(1/2, 1/2, 1/2)_{PC}$ is expected for *Cc* structure. Dashed rectangle in the inset (f) of the Fig.2(a) shows some possible diffraction data corresponding to the superlattice reflection of $(3/2, 1/2, 1/2)_{PC}$ but it is too weak to be well distinguished from the background data. Because these superlattice reflections result from oxygen octahedra rotation and are relatively weak, it is exceedingly difficult to observe using x-ray. Thus, it is difficult to distinguish the *Cc* and *R3c* structures by measuring superlattice reflections using x-ray. Though the x-ray data favor *Cc* structure for both NBT single crystals and ceramics, neutron diffraction data for NBT single crystals showed a very weak superlattice reflection near $(1/2, 1/2, 1/2)_{PC}$ which always had an offset from the calculated position. (44) This discrepancy was explained that the *Cc* structure may only exist near-surface regions of NBT crystal but the bulk NBT may still be *R3c* structure, (44) which was so called skin effect as it was observed in Pb-based relaxors. (45) This may explain the absence of $(1/2, 1/2, 1/2)_{PC}$ superlattice reflection in the inset (e) of the Fig.2(a) because the penetration depth of our lab x-ray in NBT is only $\sim 10\mu\text{m}$. (45)

Monoclinic phases were reported near rhombohedral-tetragonal MPBs in Pb-based solid solutions which were believed to be important for realizing high piezoelectricity. (18, 19) However, only a few publications reported the monoclinic phases in NBT (24, 26, 46) or $\text{K}_{0.5}\text{Na}_{0.5}\text{NbO}_3$ -based lead-free piezoelectric materials. (47) These monoclinic phases have different space groups, such as *Pm*, *Cm* and *Cc*. In order to make a comparison between Pb-based and Pb-free piezoelectric materials with monoclinic phases, the monoclinic lattice parameters compiled from references and in this work were normalized to perovskite cubic unit cell with $\alpha=\gamma=90^\circ$ and $\beta\neq 90^\circ$, as shown in Fig.3. The lattice parameters of PbZrO_3 , (48) $\text{Pb}(\text{Zn}_{1/3}\text{Nb}_{2/3})\text{O}_3$, (45) $\text{Pb}(\text{Mg}_{1/3}\text{Nb}_{2/3})\text{O}_3$, (49) BaTiO_3 , (50) and PbTiO_3 (51) which were end members for solid solutions with high piezoelectricity were also plotted in the Fig.3. The space group for each material at room temperature was marked near the data point as shown

in the Fig.3(a). The structures of $\text{Pb}(\text{Mg}_{1/3}\text{Nb}_{2/3})\text{O}_3$ and $\text{Pb}(\text{Zn}_{1/3}\text{Nb}_{2/3})\text{O}_3$ were designated as pseudo-cubic because there were no obvious phase transformation in these two relaxors. (7, 45) For Pb-based materials, several features can be seen in the Fig.3. First, PbTiO_3 is a common right end member for high piezoelectric Pb-based solid solutions, such as PbZrO_3 - PbTiO_3 , (52) $\text{Pb}(\text{Zn}_{1/3}\text{Nb}_{2/3})\text{O}_3$ - PbTiO_3 (19, 53, 54) and $\text{Pb}(\text{Mg}_{1/3}\text{Nb}_{2/3})\text{O}_3$ - PbTiO_3 (16, 17, 55-57). Comparisons between PbTiO_3 and the left end members in these Pb-base solid solutions reveal strong differences in anisotropy of the lattice parameters as shown in the Fig.3(a). PbTiO_3 shows strong anisotropy with $c/a=1.064$ while PbZrO_3 , $\text{Pb}(\text{Zn}_{1/3}\text{Nb}_{2/3})\text{O}_3$ and $\text{Pb}(\text{Mg}_{1/3}\text{Nb}_{2/3})\text{O}_3$ show weak anisotropy with $a/c=1.012$, 1 and 1, respectively. Second, the normalized cell volume decreases from the left end members to the right end member, i.e. $\text{PbZrO}_3 > \text{Pb}(\text{Zn}_{1/3}\text{Nb}_{2/3})\text{O}_3 > \text{Pb}(\text{Mg}_{1/3}\text{Nb}_{2/3})\text{O}_3 > \text{PbTiO}_3$. The cell volume of the solid solutions lies between its left and right end members. Third, a comparison of normalized monoclinic angle β reveals that Pb-based relaxor solid solutions with β larger than 90° possess higher piezoelectricity than that with β smaller than 90° , as shown in the Fig.3(b). The space groups for those Pb-based relaxor solid solutions with higher piezoelectricity are *Pm* and their lattice parameters show higher anisotropy, compared with that of lower piezoelectric materials having *Cm* space groups (see Fig.3a).

The monoclinic lattice parameters of Pb-free piezoelectric materials, such as non-relaxor KNN-LN, (47) relaxors NBT and NBBT95/5 (26) were also plotted in the Fig.3. The lattice parameters and cell volume show sharp decrease from Pb-based piezoelectric materials to Pb-free piezoelectric materials. For KNN-LN ceramics, the monoclinic angle β is larger than 90° and the lattice parameters having large anisotropy ($a/b=1.018$) are close to those of Pb-based materials with *Pm* space groups. Such characteristic of lattice parameters in Pb-based materials brings high piezoelectricity as mentioned above. We speculate this may be true for KNN-based materials because piezoelectric constant d_{33} as high as 570 pC/N had been obtained in modified KNN-based ceramics (58) and the d_{33} value was even enhanced to 700 pC/N in KNN-based textured ceramics. (59) This speculation can also be used for

NBT-based materials. As can be seen in the Fig.3, on the contrary to Pb-based solid solutions, NBT-BT lead-free solid solution has left end member of NBT with smaller cell volume than that of the right end member of BT, which makes the cell volume and lattice parameters of NBT-BT solid solutions to be small and less anisotropy. The monoclinic angle β for NBT-BT solid solution is smaller than 90° which is close to that of Pb-based relaxor solid solutions with Cm space group. The highest piezoelectric constant d_{33} reported for NBT-BT in literatures was 322 pC/N for textured ceramics (60) and 483 pC/N for single crystals. (61) The strong tetragonality of right end member in solid solutions play an important role in stabilize the monoclinic Pm phase as it can be seen in the PMN-PT solid solutions. Piezoelectric properties of NBT-based materials might be further enhanced by adjusting its lattice parameters into the characteristic of Pm space group and $\beta > 90^\circ$ via composition modification as it was in PMN-PT solid solutions.

(2). Influence of octahedron rotations on dielectric properties in relaxors

Figures 4(a) and 4(b) show the dielectric constant ϵ_r and loss factor $\tan\delta$ as a function of temperature for NBT ceramics and crystal, taken on heating. The results reveal a diffuse phase transformation with a broad dielectric maximum near $T_m=330^\circ\text{C}$ for both NBT ceramics and crystal, near and just below which the dielectric constant was frequency independent. Below a lower temperature of $T_{\text{hump}} (<T_m)$, the dielectric constant exhibited a strongly frequency dependent anomaly. The characteristic of the dielectric property for NBT reported here is similar to that reported in literatures. (40, 62) The dielectric anomaly near T_{hump} has been attributed to the thermal evolution of polar nano-regions from $R3c$ to $P4bm$ symmetries, (40) in which oxygen octahedron rotations changed from a^-a^- (Glazer notation (23)) to $a^0a^0c^+$ (Glazer notation (23)). However, random electric fields in NBT arising from heterovalent cations Na^+ and Bi^{3+} on A sites of perovskite also play important role in forming PNRs which lead to the relaxor behavior in NBT. (44) It was believed that the random electric fields in PZT solid solutions were very weak because the B sites of perovskite are occupied by homovalent cations Zr^{4+} and Ti^{4+} . (9) The oxygen octahedral rotations will appear in PZT solid solutions when it enters the low

This article is protected by copyright. All rights reserved

temperature phase field.(27, 30) This disordered nonpolar oxygen octahedral rotations result in random strains which may disrupt the long range polar order in PZT.(30) Such coupling between the polarizations and the oxygen octahedral rotations results in fluctuation effects in the polarization characterized by frequency dispersion of the dielectric constant in PZT55/45 ceramics, as shown in Fig.4(c). Comparison of Figs.4(a) and 4(c) reveals that both NBT and PZT55/45 ceramics show dielectric dispersion below the temperature of T_{hump} and the dispersion disappear above T_{hump} . These results indicate that the oxygen octahedral rotations might play important role in enhancing dielectric dispersion in NBT. Fig.4(d) shows the dielectric constant ϵ_r and loss factor $\tan\delta$ for typical relaxor ferroelectric PMNT72/28 ceramics in which random electric fields supposed to be stronger than that in PZT due to the heterovalent cations Nb^{5+} and Mg^{2+} on B sites of perovskite. The T_m occurs around 120°C and shifts to high temperature with increasing frequency.

Figure 5 (a) shows the dielectric constant ϵ_r as a function of frequency at 30 °C for NBT, PMNT72/28 and PZT55/45. The dielectric constant ϵ_r of PMNT72/28 is ~ 4 times larger than that of NBT and PZT55/45 and shows strong frequency dependent behavior when the measured frequencies increases from 100 Hz to 1MHz. However, the ϵ_r for NBT and PZT55/45 show moderate and weak frequency dependent behavior. These results indicate that both random electric fields and oxygen octahedron rotations can cause frequency dispersion on dielectric properties in ferroelectrics. However, the frequency dispersion caused by oxygen octahedron rotations is much weaker than that of caused by the random electric fields.

Figure 5(b) shows the dielectric constant changing rate of $-\Delta\epsilon_r/\Delta f$ ($f= 10$ kHz and 100 kHz) as a function of temperature for NBT, PMNT72/28 and PZT55/45, respectively. The $-\Delta\epsilon_r/\Delta f$ for PMNT72/28 increases very fast with increasing temperature toward T_m compared with that for NBT, while the $-\Delta\epsilon_r/\Delta f$ for PZT55/45 decreases with increasing temperature, as shown in the Fig.5(b). Comparison of the $-\Delta\epsilon_r/\Delta f$ for PZT55/45 and PMNT72/28 reveals that the coupling between the polarizations and the oxygen octahedral rotations through random strains is weaker than the coupling between the polarizations and the random electric fields. For NBT, This article is protected by copyright. All rights reserved

the coupling between the polarizations and the random electric fields might be disrupted by the oxygen octahedral rotations, which might be responsible for the less frequency dispersion on dielectric properties in NBT compared with PMNT72/28.

The frequency dispersion on dielectric properties in relaxor ferroelectrics can be simulated by using multi-Debye relaxation model with Lorentzian or Gaussian distribution functions.(63, 64) This model had been used to simulate the dispersive dielectric constant below the temperature of T_{hump} in NBT-6%BT ceramics. (40) Following these works, the dielectric constant ϵ_r for NBT ceramics was deconvolved with Lorentzian function using software of OriginPro (Originlab, Inc.). Fig. 6(a) shows the deconvolution results under 10 kHz for NBT ceramics, in which the measured temperature dependent dielectric constant ϵ_r can be well described by two independent Lorentzian curves centered around T_{m1} and T_{m2} . Fig. 6(b) shows the calculated dielectric constant ϵ_r as a function of temperature under various frequencies, in which the calculated dielectric data for fit curve 1 were normalized according to the highest temperature (350 °C) data measured under 10 kHz. The fitted T_{m1} and T_{m2} were listed in Table III. Please note that the T_{m1} for fit curve 1 shifted towards high temperature with increasing frequency, which is typical relaxor characteristic. However, the T_{m2} for fit curve 2 is independent on the measured frequency, as shown in the Fig.6(b) and Table III.

The relaxation time in relaxor ferroelectrics can be modeled using Vogel-Fulcher relationship (8, 41, 65):

$$\omega = \omega_0 \exp[-E_a/k(T_m - T_f)] \quad (1)$$

where ω_0 , E_a , k , T_m and T_f are the Debye frequency, the activation energy, the Boltzman constant, the temperature of the dielectric maximum occurred at measured frequency ω and static freezing temperature. Fig.7(a) shows the Vogel-Fulcher fitting plot according to the equation (1) using the deconvolved T_{m1} data listed in the Table III. The best fit was obtained with $\omega_0 = 5.21 \times 10^{13}$ Hz, $E_a = 0.1488$ eV and $T_f = 404.91$ K. The linear dependence between $\ln \omega$ and $1/(T_{m1} - 404.91)$ shown in Fig.7(b) indicates the deconvolved fit curve 1 in the Fig.6 can be well described using Vogel-Fulcher relationship. The implication is that the relaxor behavior in NBT ceramics below

T_{hump} results from polar nanoregions due to the coupling between random electric fields and spontaneous polarization of monoclinic phase with $a^-a^-c^-$ oxygen octahedral rotations. However, the $a^-a^-c^-$ oxygen octahedral rotations might have some bounding effects on the interaction between polar nanoregions, which yields high Ea compared to that of 0.0407 eV reported for PMNT90/10 ceramics.(8)

IV. Summary

Our findings demonstrate that the monoclinic structure with Cc space group can be detected in both NBT single crystal and ceramics with laboratory XRD. The diffraction profile obtained with high resolution lab XRD for NBT single crystal can be well described using Cc model instead of $R3c$ model. Our results are consistent with the high-resolution synchrotron XRD results reported previously.(24, 26) However, the superlattice $(1/2, 1/2, 1/2)_{PC}$ was not observed because the XRD is insensitive to atom position of oxygen. The contradiction between the Cc and the $R3c$ models obtained by using XRD and neutron diffraction maybe reconciled by skin effect.(44) NBT possesses the smallest lattice parameters and cell volume compared with lead-based RFs such as $Pb(Zn_{1/3}Nb_{2/3})O_3$ and $Pb(Mg_{1/3}Nb_{2/3})O_3$ which form solid solutions with $PbTiO_3$ and exhibit largest longitudinal piezoelectric coefficient d_{33} when the monoclinic phase has the Pm symmetry.

Comparing dielectric constant of NBT with that of PZT55/45 and PMNT72/28 reveals that both oxygen octahedral rotations and random electric fields play important role in the frequency dispersion of the dielectric constant for NBT. The temperature dependent dielectric constant for NBT can be deconvolved into two independent processes described using Lorentzian functions. The lower temperature process shows a typical relaxor characteristic and follows the Vogel-Fulcher relationship.

Acknowledgements

This work was supported by the Fundamental Research Funds for the Central Universities, JLU under 1018320174002 (W. Ge), by the Department of Energy under DE-FG02-07ER46480 (DV), by the Provincial Natural Science Foundation of Jilin
This article is protected by copyright. All rights reserved

under Grant No. 20190201106JC (X. Liu), by the Natural Science Foundation of Shanghai under Grants No. 19ZR1436200 and 19440760800 (X. Li).

Author Manuscript

Reference

1. Takenaka T, Maruyama K, Sakata K. $\text{Na}_{0.5}\text{Bi}_{0.5}\text{TiO}_3\text{-BaTiO}_3$ system for lead-free piezoelectric ceramics. *Japanese Journal of Applied Physics*. 1991;30(9B):2236-9.
2. Liu X, Tan X. Giant Strains in Non-Textured $(\text{Bi}_{1/2}\text{Na}_{1/2})\text{TiO}_3$ -Based Lead-Free Ceramics. *Adv Mater*. 2016;28(3):574-8.
3. Dittmer R, Jo W, Rödel J, Kalinin S, Balke N. Nanoscale Insight Into Lead-Free BNT-BT-xKNN. *Adv Funct Mater*. 2012;22(20):4208-15.
4. Zhang QH, Zhang YY, Wang FF, Wang YJ, Lin D, Zhao XY, et al. Enhanced piezoelectric and ferroelectric properties in Mn-doped $\text{Na}_{0.5}\text{Bi}_{0.5}\text{TiO}_3\text{-BaTiO}_3$ single crystals. *Appl Phys Lett*. 2009;95(10).
5. Park SE, Shrout TR. Ultrahigh strain and piezoelectric behavior in relaxor based ferroelectric single crystals. *Journal of Applied Physics*. 1997;82(4):1804-11.
6. Guo YP, Luo HS, Ling D, Xu HQ, He TH, Yin ZW. The phase transition sequence and the location of the morphotropic phase boundary region in $(1-x)[\text{Pb}(\text{Mg}_{1/3}\text{Nb}_{2/3})\text{O}_3]\text{-xPbTiO}_3$ single crystal. *J Phys-Condens Mat*. 2003;15(2):L77-L82.
7. Cross LE. Relaxor ferroelectrics. *Ferroelectrics*. 1987; 76(1):241-67.
8. Viehland D, Jang SJ, Cross LE, Wuttig M. Freezing of the Polarization Fluctuations in Lead Magnesium Niobate Relaxors. *Journal of Applied Physics*. 1990;68(6):2916-21.
9. Phelan D, Stock C, Rodriguez-Rivera JA, Chi SX, Leao J, Long XF, et al. Role of random electric fields in relaxors. *P Natl Acad Sci USA*. 2014;111(5):1754-9.
10. Burns G, Dacol FH. Glassy Polarization Behavior in Ferroelectric Compounds $\text{Pb}(\text{Mg}_{1/3}\text{Nb}_{2/3})\text{O}_3$ and $\text{Pb}(\text{Zn}_{1/3}\text{Nb}_{2/3})\text{O}_3$. *Solid State Communications*. 1983;48(10):853-6.
11. Viehland D, Jang SJ, Cross LE, Wuttig M. Deviation from Curie-Weiss Behavior in Relaxor Ferroelectrics. *Physical Review B*. 1992;46(13):8003-6.
12. Gehring PM, Hiraka H, Stock C, Lee SH, Chen W, Ye ZG, et al. Reassessment of the Burns temperature and its relationship to the diffuse scattering, lattice dynamics, and thermal expansion in relaxor $\text{Pb}(\text{Mg}_{1/3}\text{Nb}_{2/3})\text{O}_3$. *Physical Review B*. 2009;79(22):224109.
13. Sakata K, Masuda Y. Ferroelectric and antiferroelectric properties of $(\text{Na}_{0.5}\text{Bi}_{0.5})\text{TiO}_3\text{-SrTiO}_3$ solid solution ceramics. *Ferroelectrics*. 1974;7:347-9.
14. Stock C, Xu GY, Gehring PM, Luo H, Zhao X, Cao H, et al. Neutron and x-ray diffraction study

of cubic [111] field-cooled $\text{Pb}(\text{Mg}_{1/3}\text{Nb}_{2/3})\text{O}_3$. *Physical Review B*. 2007;76(6):-.

15. Choi SW, Shrout TR, Jang SJ, Bhalla AS. Morphotropic Phase-Boundary in $\text{Pb}(\text{Mg}_{1/3}\text{Nb}_{2/3})\text{O}_3$ - PbTiO_3 System. *Mater Lett*. 1989;8(6-7):253-5.

16. Noheda B, Cox DE, Shirane G, Gao J, Ye ZG. Phase diagram of the ferroelectric relaxor $(1-x)\text{PbMg}_{1/3}\text{Nb}_{2/3}\text{O}_3$ - $x\text{PbTiO}_3$. *Physical Review B*. 2002;66(5):054104.

17. Cao H, Li JF, Viehland D, Xu GY. Fragile phase stability in $(1-x)\text{Pb}(\text{Mg}_{1/3}\text{Nb}_{2/3}\text{O}_3)$ - $x\text{PbTiO}_3$ crystals: A comparison of [001] and [110] field-cooled phase diagrams. *Physical Review B*. 2006;73(18):184110.

18. Fu HX, Cohen RE. Polarization rotation mechanism for ultrahigh electromechanical response in single-crystal piezoelectrics. *Nature*. 2000;403(6767):281-3.

19. Noheda B, Cox DE, Shirane G, Park SE, Cross LE, Zhong Z. Polarization rotation via a monoclinic phase in the piezoelectric 92% $\text{PbZn}_{1/3}\text{Nb}_{2/3}\text{O}_3$ -8% PbTiO_3 . *Physical Review Letters*. 2001;86(17):3891-4.

20. Noheda B. Structure and high-piezoelectricity in lead oxide solid solutions. *Curr Opin Solid St M*. 2002;6(1):27-34.

21. Noheda B, Cox DE. Bridging phases at the morphotropic boundaries of lead oxide solid solutions. *Phase Transitions*. 2006;79(1-2):5-20.

22. Jones GO, Thomas PA. Investigation of the structure and phase transitions in the novel A-site substituted distorted perovskite compound $\text{Na}_{0.5}\text{Bi}_{0.5}\text{TiO}_3$. *Acta Crystallogr B*. 2002;58:168-78.

23. Glazer A. The classification of tilted octahedra in perovskites. *Acta Crystallographica Section B*. 1972;28(11):3384-92.

24. Aksel E, Forrester JS, Jones JL, Thomas PA, Page K, Suchomel MR. Monoclinic crystal structure of polycrystalline $\text{Na}_{0.5}\text{Bi}_{0.5}\text{TiO}_3$. *Appl Phys Lett*. 2011;98(15):152901.

25. Aksel E, Forrester JS, Kowalski B, Jones JL, Thomas PA. Phase transition sequence in sodium bismuth titanate observed using high-resolution x-ray diffraction. *Appl Phys Lett*. 2011;99(22):222901-3.

26. Ge W, Luo C, Zhang Q, Ren Y, Li J, Luo H, et al. Evolution of structure in $\text{Na}_{0.5}\text{Bi}_{0.5}\text{TiO}_3$ single crystals with BaTiO_3 . *Appl Phys Lett*. 2014;105(16):162913.

27. Ranjan R, Singh AK, Ragini, Pandey D. Comparison of the Cc and R3c space groups for the superlattice phase of $\text{Pb}(\text{Zr}_{0.52}\text{Ti}_{0.48})\text{O}_3$. *Physical Review B*. 2005;71(9).

This article is protected by copyright. All rights reserved

28. Janolin PE, Dkhil B, Bouvier P, Kreisel J, Thomas PA. Pressure instabilities up to 46GPa in the relaxor ferroelectric $\text{PbZn}_{1/3}\text{Nb}_{2/3}\text{O}_3$. *Physical Review B*. 2006;73(9):094128.
29. Janolin PE, Bouvier P, Kreisel J, Thomas PA, Kornev IA, Bellaiche L, et al. High-Pressure Effect on PbTiO_3 : An Investigation by Raman and X-Ray Scattering up to 63 GPa. *Physical Review Letters*. 2008;101(23).
30. Dai XH, Xu ZK, Viehland D. Effect of Oxygen Octahedron Rotations on the Phase-Stability, Transformational Characteristics, and Polarization Behavior in the Lead-Zirconate-Titanate Crystalline Solution Series. *J Am Ceram Soc*. 1995;78(10):2815-27.
31. Vugmeister BE, Glinchuk MD. Dipole glass and ferroelectricity in random-site electric dipole systems. *Rev Mod Phys*. 1990;62(4):993-1026.
32. Westphal V, Kleemann W, Glinchuk MD. Diffuse phase transitions and random-field-induced domain states of the "relaxor" ferroelectric $\text{PbMg}_{1/3}\text{Nb}_{2/3}\text{O}_3$. *Physical Review Letters*. 1992;68(6):847.
33. Stock C, Birgeneau RJ, Wakimoto S, Gardner JS, Chen W, Ye ZG, et al. Universal static and dynamic properties of the structural transition in $\text{Pb}(\text{Zn}_{1/3}\text{Nb}_{2/3})\text{O}_3$. *Physical Review B*. 2004;69(9):094104.
34. Tinte S, Burton B, Cockayne E, Waghmare U. Origin of the Relaxor State in $\text{Pb}(\text{BxB}_{1-x})\text{O}_3$ Perovskites. *Physical Review Letters*. 2006;97(13).
35. Cowley RA, Gvasaliya SN, Lushnikov SG, Roessli B, Rotaru GM. Relaxing with relaxors: a review of relaxor ferroelectrics. *Advances in Physics*. 2011;60(2):229-327.
36. Pirc R, Blinc R. Spherical random-bond-random-field model of relaxor ferroelectrics. *Physical Review B*. 1999;60(19):13470-8.
37. Grinberg I, Juhás P, Davies PK, Rappe AM. Relationship between Local Structure and Relaxor Behavior in Perovskite Oxides. *Physical Review Letters*. 2007;99(26):267603.
38. Akbarzadeh AR, Prosandeev S, Walter EJ, Al-Barakaty A, Bellaiche L. Finite-Temperature Properties of $\text{Ba}(\text{Zr},\text{Ti})\text{O}_3$ Relaxors from First Principles. *Physical Review Letters*. 2012;108(25):257601.
39. Maier BJ, Angel RJ, Marshall WG, Mihailova B, Paulmann C, Engel JM, et al. Octahedral tilting in Pb-based relaxor ferroelectrics at high pressure. *Acta Crystallogr B*. 2010;66:280-91.
40. Jo W, Schaab S, Sapper E, Schmitt LA, Kleebe H-J, Bell AJ, et al. On the phase identity and its

thermal evolution of lead free $(\text{Bi}_{1/2}\text{Na}_{1/2})\text{TiO}_3$ -6 mol% BaTiO_3 . *Journal of Applied Physics*. 2011;110(7):074106.

41. Ranjan R, Dviwedi A. Structure and dielectric properties of $(\text{NaBi})\text{BaTiO}_3$: $0 \leq x \leq 0.10$. *Solid State Communications*. 2005;135(6):394-9.
42. Swartz SL, Shrout TR. Fabrication of Perovskite Lead Magnesium Niobate. *Mater Res Bull*. 1982;17(10):1245-50.
43. Zhang QH, Zhang YY, Wang FF, Wang YJ, Lin D, Zhao XY, et al. Enhanced piezoelectric and ferroelectric properties in Mn-doped $\text{Na}_0.5\text{Bi}_0.5\text{TiO}_3$ - BaTiO_3 single crystals. *Appl Phys Lett*. 2009;95(10):102904, 3pp.
44. Ge W, Devreugd CP, Phelan D, Zhang Q, Ahart M, Li J, et al. Lead-free and lead-based ABO_3 perovskite relaxors with mixed-valence A-site and B-site disorder: Comparative neutron scattering structural study of $(\text{Na}_{1/2}\text{Bi}_{1/2})\text{TiO}_3$ and $\text{Pb}(\text{Mg}_{1/3}\text{Nb}_{2/3})\text{O}_3$. *Physical Review B*. 2013;88(17):174115.
45. Xu GY, Zhong Z, Bing Y, Ye ZG, Stock C, Shirane G. Ground state of the relaxor ferroelectric $\text{Pb}(\text{Zn}_{1/3}\text{Nb}_{2/3})\text{O}_3$. *Physical Review B*. 2003;67(10):104102.
46. Gorfman S, Thomas PA. Evidence for a non-rhombohedral average structure in the lead-free piezoelectric material $\text{Na}_0.5\text{Bi}_0.5\text{TiO}_3$. *J Appl Crystallogr*. 2010;43(6):1409-14.
47. Ge W, Ren Y, Zhang J, Devreugd CP, Li J, Viehland D. A monoclinic-tetragonal ferroelectric phase transition in lead-free $(\text{K}_{0.5}\text{Na}_{0.5})\text{NbO}_3$ - $x\%\text{LiNbO}_3$ solid solution. *Journal of Applied Physics*. 2012;111(10):103503.
48. Teslic S, Egami T. Atomic Structure of PbZrO_3 Determined by Pulsed Neutron Diffraction. *Acta Crystallographica Section B*. 1998;54(6):750-65.
49. Verbaere A, Piffard Y, Ye ZG, Husson E. Lead Magnoniobate Crystal-Structure Determination. *Mater Res Bull*. 1992;27(10):1227-34.
50. Buttner RH, Maslen EN. Structural parameters and electron difference density in BaTiO_3 . *Acta Crystallographica Section B*. 1992;48(6):764-9.
51. Nelmes RJ, Kuhs WF. The crystal structure of tetragonal PbTiO_3 at room temperature and at 700 K. *Solid State Communications*. 1985;54(8):721-3.
52. Noheda B, Cox DE, Shirane G, Guo R, Jones B, Cross LE. Stability of the monoclinic phase in the ferroelectric perovskite $\text{PbZr}_{1-x}\text{Ti}_x\text{O}_3$. *Physical Review B*. 2001;63(1):014103.
53. Noheda B, Zhong Z, Cox DE, Shirane G, Park SE, Rehrig P. Electric-field-induced phase

transitions in rhombohedral $\text{Pb}(\text{Zn}_{1/3}\text{Nb}_{2/3})(1-x)\text{Ti}_x\text{O}_3$. *Physical Review B*. 2002;65(22):224101.

54. Uesu Y, Matsuda M, Yamada Y, Fujishiro K, Cox DE, Noheda B, et al. Symmetry of high-piezoelectric Pb-based complex perovskites at the morphotropic phase boundary: I. Neutron diffraction study on $\text{Pb}(\text{Zn}_{1/3}\text{Nb}_{2/3})\text{O}-3-9\%\text{PbTiO}_3$. *J Phys Soc Jpn*. 2002;71(3):960-5.

55. Cao H, Li JF, Viehland D. Structural origin of the relaxor-to-normal ferroelectric transition in $\text{Pb}(\text{Mg}_{1/3}\text{Nb}_{2/3}\text{O}_3)_x\text{PbTiO}_3$. *Journal of Applied Physics*. 2006;100(3):034110.

56. Bai FM, Wang NG, Li JF, Viehland D, Gehring PM, Xu GY, et al. X-ray and neutron diffraction investigations of the structural phase transformation sequence under electric field in $0.7\text{Pb}(\text{Mg}_{1/3}\text{Nb}_{2/3})-0.3\text{PbTiO}_3$ crystal. *Journal of Applied Physics*. 2004;96(3):1620-7.

57. Cao H, Li JF, Viehland D. Electric-field-induced orthorhombic to monoclinic M-B phase transition in [111] electric field cooled $\text{Pb}(\text{Mg}_{1/3}\text{Nb}_{2/3}\text{O}_3)-30\%\text{PbTiO}_3$ crystals. *Journal of Applied Physics*. 2006;100(8):084102.

58. Xu K, Li J, Lv X, Wu JG, Zhang XX, Xiao DQ, et al. Superior Piezoelectric Properties in Potassium-Sodium Niobate Lead-Free Ceramics. *Adv Mater*. 2016;28(38):8519-23.

59. Li P, Zhai J, Shen B, Zhang S, Li X, Zhu F, et al. Ultrahigh Piezoelectric Properties in Textured $(\text{K},\text{Na})\text{NbO}_3$ -Based Lead-Free Ceramics. *Adv Mater*. 2018.

60. Maurya D, Zhou Y, Yan Y, Priya S. Synthesis mechanism of grain-oriented lead-free piezoelectric $\text{Na}_{0.5}\text{Bi}_{0.5}\text{TiO}_3\text{-BaTiO}_3$ ceramics with giant piezoelectric response. *Journal of Materials Chemistry C*. 2013;1(11):2102.

61. Zhang QH, Zhang YY, Wang FF, Wang YJ, Lin D, Zhao XY, et al. Enhanced piezoelectric and ferroelectric properties in Mn-doped $\text{Na}_{0.5}\text{Bi}_{0.5}\text{TiO}_3\text{-BaTiO}_3$ single crystals. *Appl Phys Lett*. 2009;95(10):102904.

62. Wylie-van Eerd B, Damjanovic D, Klein N, Setter N, Trodahl J. Structural complexity of $(\text{Na}_{0.5}\text{Bi}_{0.5})\text{TiO}_3\text{-BaTiO}_3$ as revealed by Raman spectroscopy. *Physical Review B*. 2010;82(10).

63. García Zaldívar O, Peláiz-Barranco A, Calderón-Piñar F, López-Noda R, Velazco-Molina L. A relaxation model by using a relaxation times distribution for relaxor ferroelectrics. *Scripta Mater*. 2006;55(10):927-30.

64. Lin H-T, Van Aken DC, Huebner W. Modeling the Dielectric Response and Relaxation Spectra of Relaxor Ferroelectrics. *J Am Ceram Soc*. 1999;82(10):2698-704.

65. Tagantsev AK. Vogel-Fulcher relationship for the dielectric permittivity of relaxor ferroelectrics.

Author Manuscript

Table I XRD peak fitting results for NBT crystal according to monoclinic Cc structure

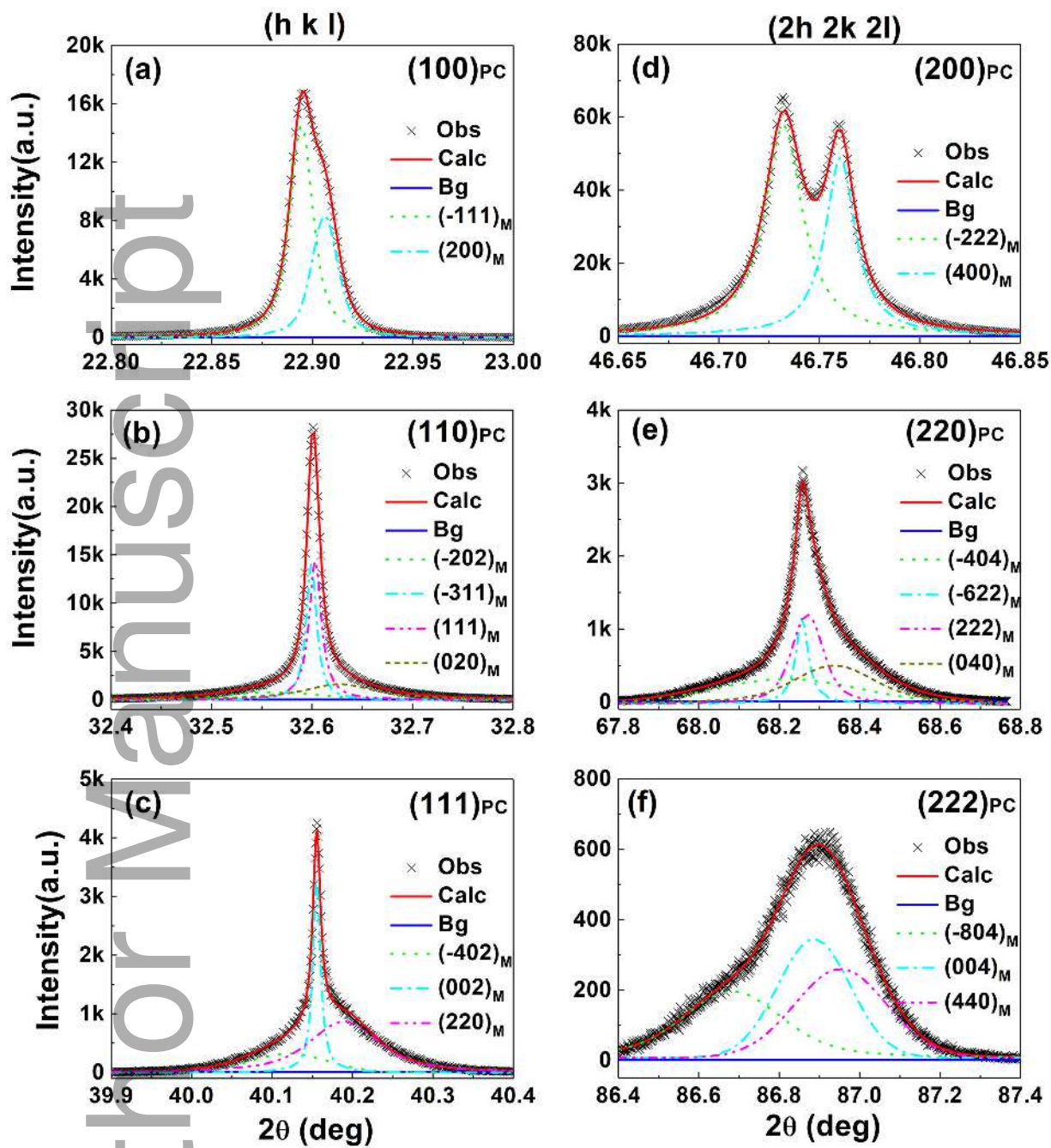
| h k l | $2\theta_{hkl}$ (°) | d_{hkl} (Å) | $2\theta_{2h2k2l}$ (°) | d_{2h2k2l} (Å) | d_{hkl}/d_{2h2k2l} |
|--------------------|--|---------------|------------------------|------------------|----------------------|
| -1 1 1 | 22.8946 | 3.8813 | 46.7322 | 1.9422 | 1.9983 |
| 2 0 0 | 22.9061 | 3.8793 | 46.7605 | 1.9411 | 1.9985 |
| -2 0 2 | 32.5596 | 2.7478 | 68.2196 | 1.3736 | 2.0004 |
| -3 1 1 | 32.5994 | 2.7446 | 68.2569 | 1.3730 | 1.9990 |
| 1 1 1 | 32.6032 | 2.7443 | 68.2701 | 1.3727 | 1.9992 |
| 0 2 0 | 32.6273 | 2.7423 | 68.3366 | 1.3716 | 1.9993 |
| -4 0 2 | 40.1210 | 2.2457 | 86.6831 | 1.1223 | 2.0009 |
| 0 0 2 | 40.1554 | 2.2438 | 86.8864 | 1.1202 | 2.0031 |
| 2 2 0 | 40.1894 | 2.2420 | 86.9527 | 1.1195 | 2.0026 |
| (a, b, c, β) | (9.5201 Å, 5.4846 Å, 5.5024 Å, 125.3542 °) | | | | |

Table II XRD peak fitting results for NBT ceramics according to monoclinic Cc structure

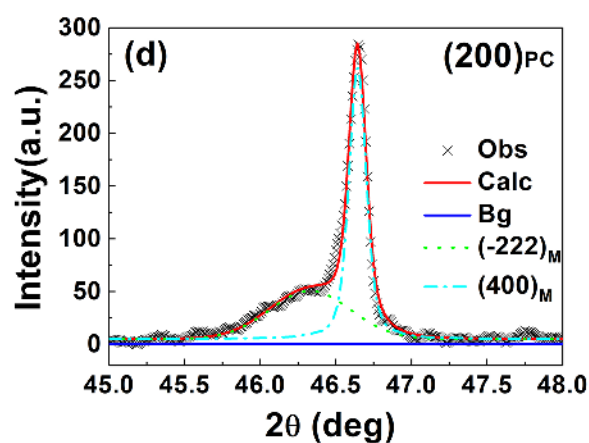
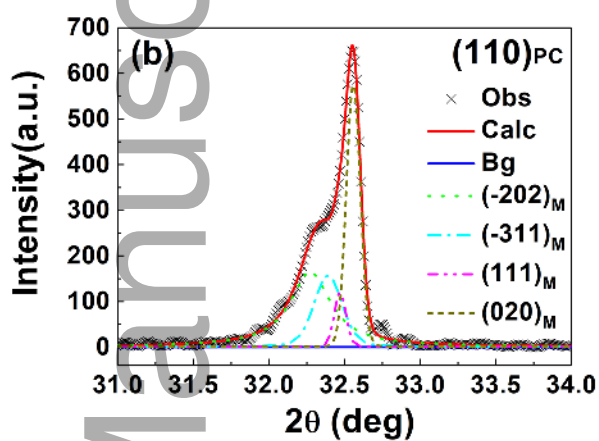
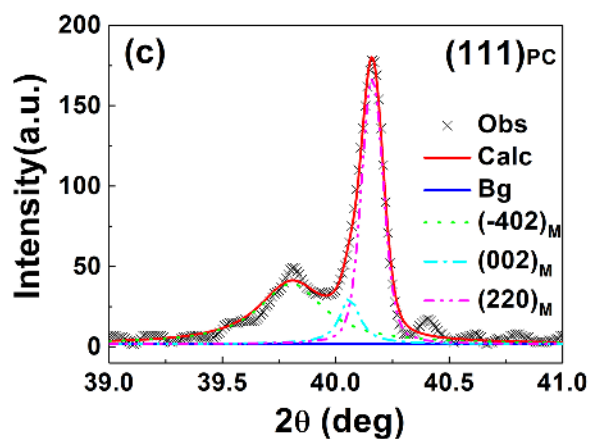
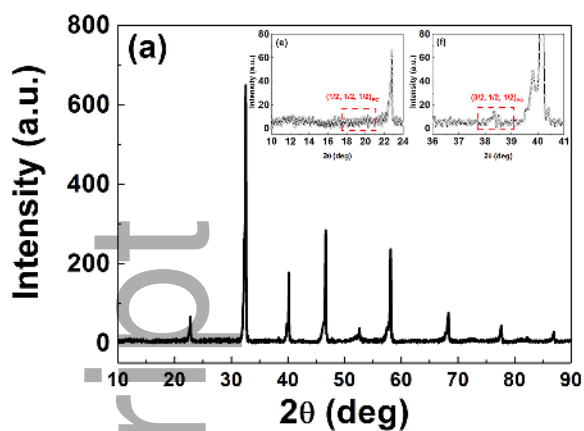
| h k l | $2\theta_{\text{hkl}}$ for NBT ceramics ($^{\circ}$) | d_{hkl} for NBT ceramics (\AA) | $(d_{\text{ceramic}}-d_{\text{crystal}})/d_{\text{ceramic}}$ (%) |
|--------------------|--|---|---|
| -2 0 2 | 32.27255 | 2.7716 | 0.86 |
| -3 1 1 | 32.391 | 2.7617 | 0.62 |
| 1 1 1 | 32.47044 | 2.7551 | 0.39 |
| 0 2 0 | 32.55781 | 2.7479 | 0.20 |
| -4 0 2 | 39.80381 | 2.2628 | 0.84 |
| 0 0 2 | 40.06132 | 2.2488 | 0.22 |
| 2 2 0 | 40.1612 | 2.2435 | 0.049 |
| -2 2 2 | 46.33032 | 1.9581 | 0.81 |
| 4 0 0 | 46.64422 | 1.9473 | 0.31 |
| (a, b, c, β) | $(9.6660 \text{ \AA}, 5.4958 \text{ \AA}, 5.5815 \text{ \AA}, 126.3090^{\circ})$ | | $(1.51, 0.20, 1.42, 0.76)$ |

Table III Deconvolved T_{m1} and T_{m2} for NBT ceramics under various frequencies (ω)

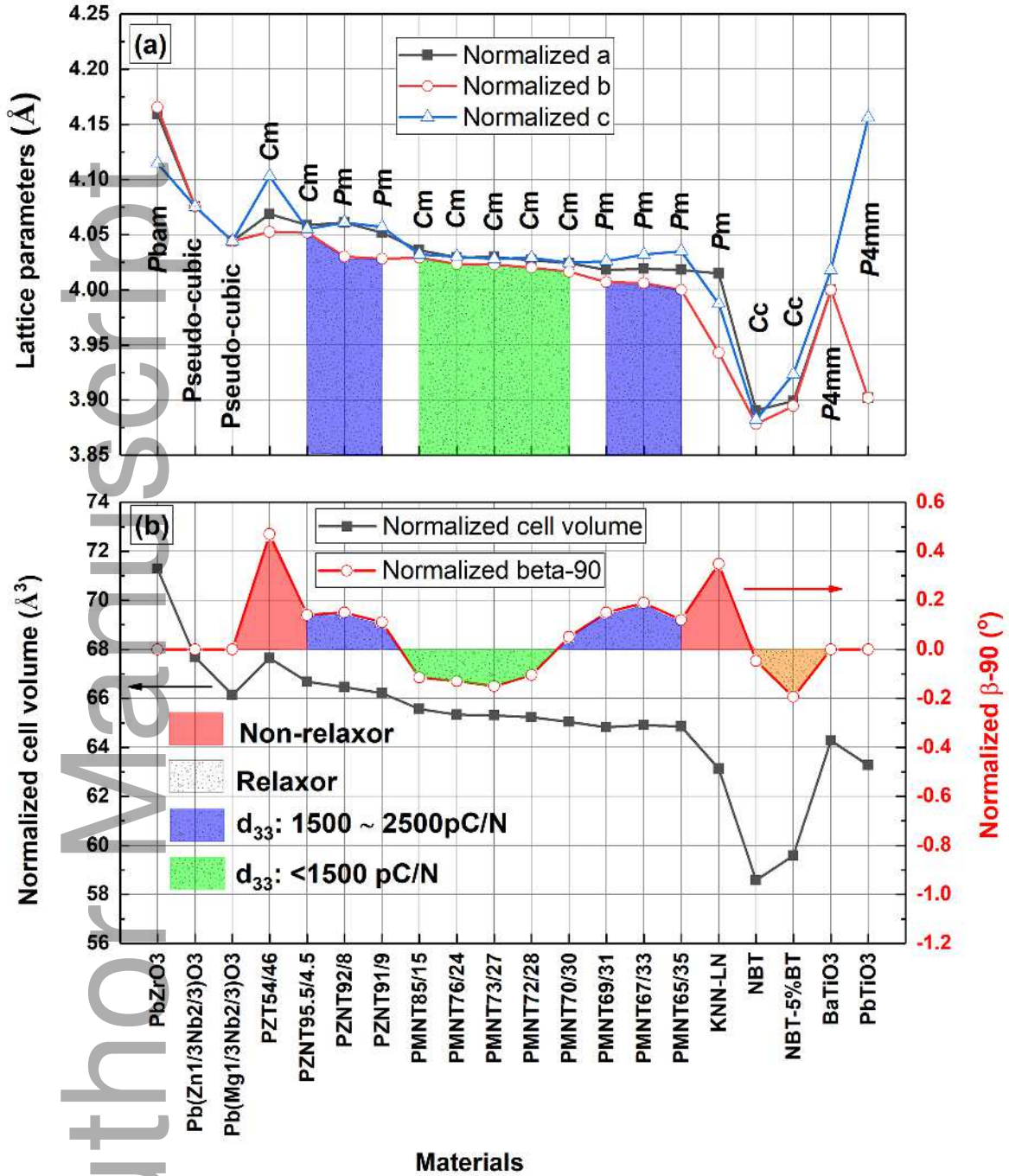
| ω (Hz) | T_{m1} (K) | T_{m2} (K) |
|---------------|--------------|--------------|
| 100 | 465.78 | 610.51 |
| 1000 | 471.03 | 609.45 |
| 10000 | 478.63 | 609.46 |
| 100000 | 490.19 | 609.17 |
| 500000 | 498.57 | 609.09 |
| 1000000 | 502.08 | 609.06 |



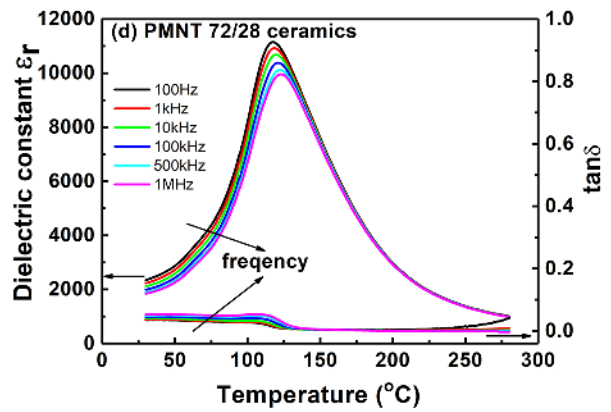
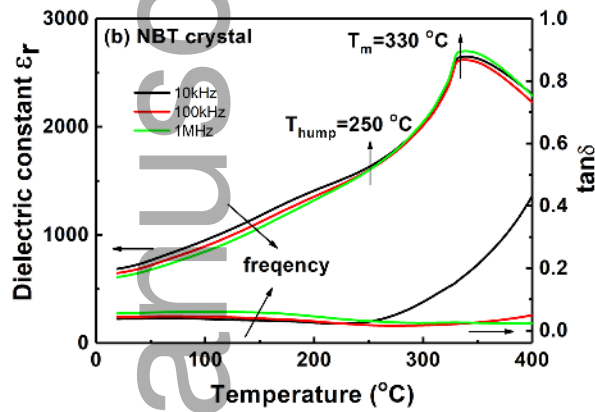
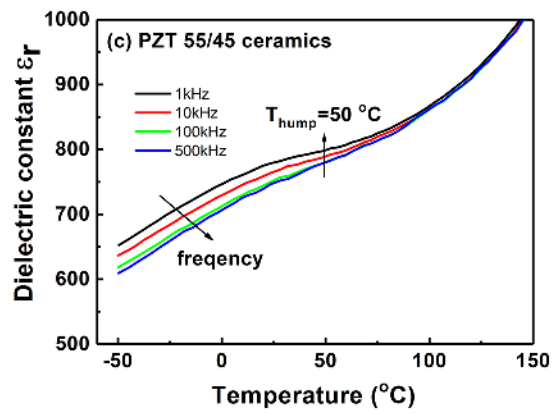
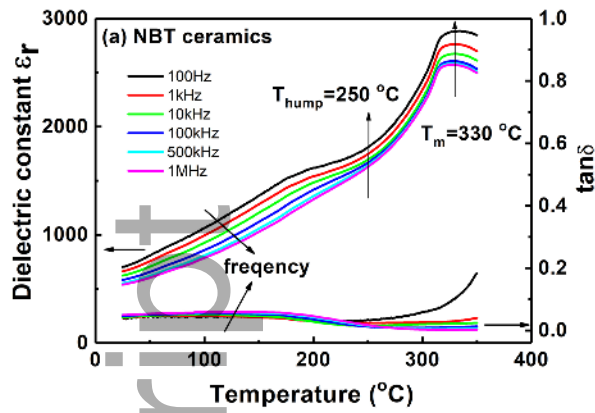
jace_16986_f1.tif



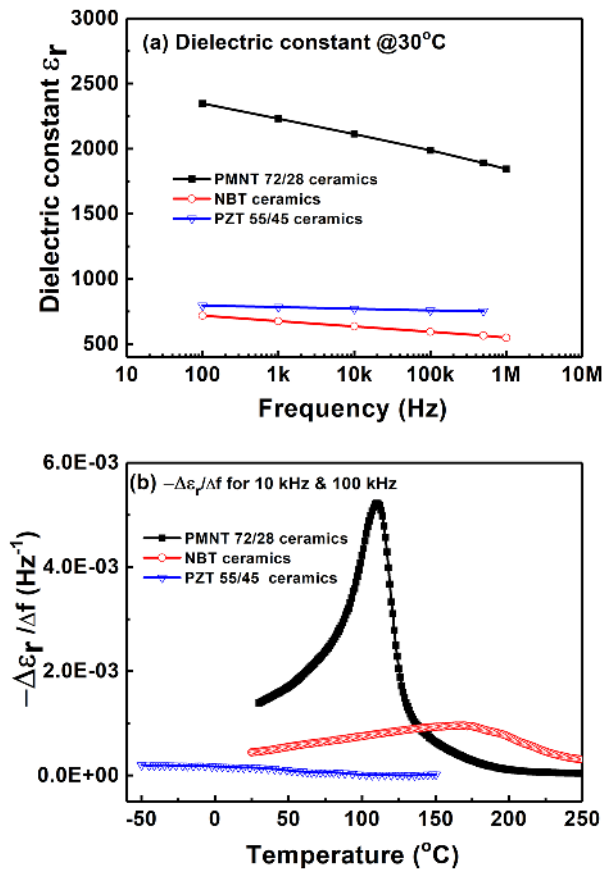
jace_16986_f2.tif



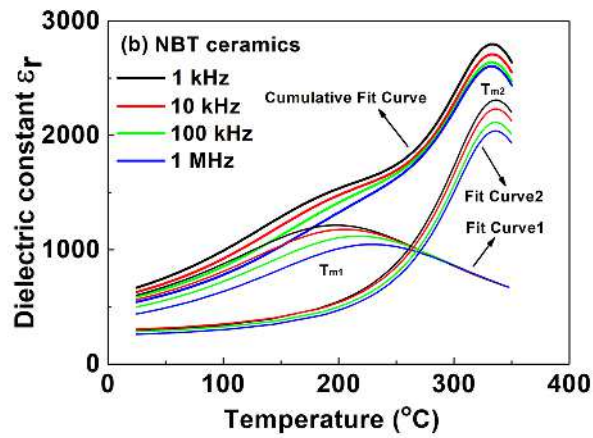
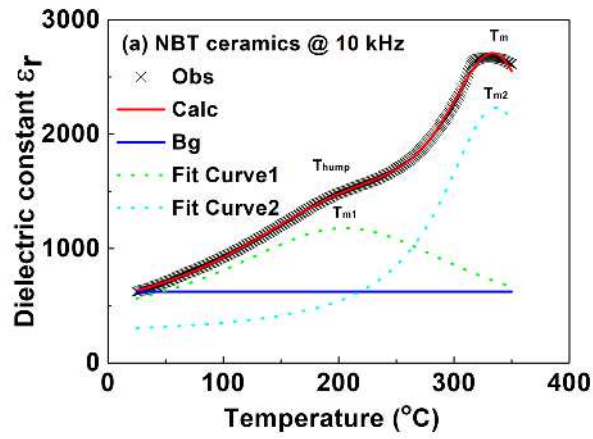
jace_16986_f3.tif



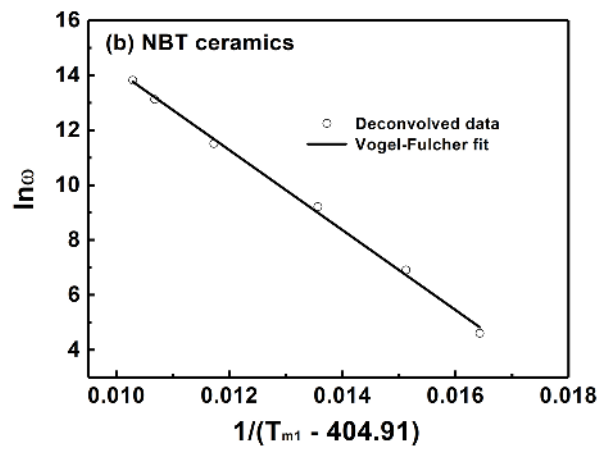
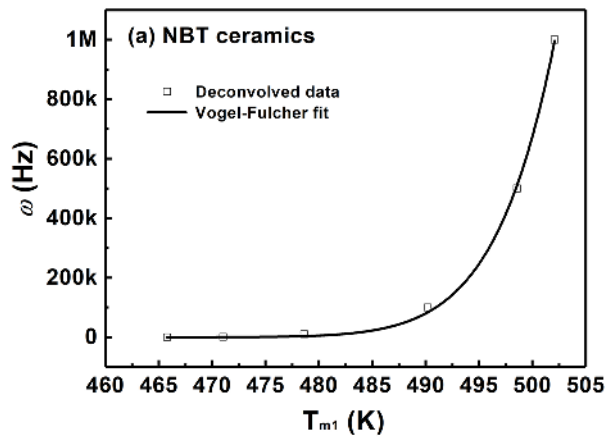
jace_16986_f4.tif



jace_16986_f5.tif



jace_16986_f6.tif



jace_16986_f7.tif